

*Erik Jonsson School of Engineering and Computer Science
Texas Analog Center of Excellence*

***Design and Demonstration of Antenna-Coupled Schottky Diodes
in a Foundry Complementary Metal-Oxide Semiconductor
Technology for Electronic Detection of Far-Infrared Radiation***

UT Dallas Author(s):

Keneth K. O

Rights:

©2019 The Authors

Citation:

Ahmad, Z., A. Lisauskas, and H. G. Roskos. 2019. "Design and demonstration of antenna-coupled Schottky diodes in a foundry complementary metal-oxide semiconductor technology for electronic detection of far-infrared radiation." *Journal of Applied Physics* 125(19): art. 194501, doi: 10.1063/1.5083689

This document is being made freely available by the Eugene McDermott Library of the University of Texas at Dallas with permission of the copyright owner. All rights are reserved under United States copyright law unless specified otherwise.

Design and demonstration of antenna-coupled Schottky diodes in a foundry complementary metal-oxide semiconductor technology for electronic detection of far-infrared radiation

Cite as: J. Appl. Phys. **125**, 194501 (2019); <https://doi.org/10.1063/1.5083689>

Submitted: 30 November 2018 . Accepted: 24 April 2019 . Published Online: 16 May 2019

Z. Ahmad , A. Lisauskas , H. G. Roskos , and K. K. O

COLLECTIONS

Paper published as part of the special topic on [Advances in Terahertz Solid-State Physics and Devices](#)

Note: This paper is part of the Special Topic section published in "Advances in terahertz solid-state physics and devices," J. Appl. Phys. **125**(15) (2019).



View Online



Export Citation



CrossMark

ARTICLES YOU MAY BE INTERESTED IN

[Terahertz emission from biased AlGaIn/GaN high-electron-mobility transistors](#)

Journal of Applied Physics **125**, 151614 (2019); <https://doi.org/10.1063/1.5083838>

[Large-scale array of resonant-tunneling-diode terahertz oscillators for high output power at 1 THz](#)

Journal of Applied Physics **125**, 151601 (2019); <https://doi.org/10.1063/1.5051007>

[Analysis of square-law detector for high-sensitive detection of terahertz waves](#)

Journal of Applied Physics **125**, 174506 (2019); <https://doi.org/10.1063/1.5083654>



Lock-in Amplifiers

Zurich Instruments

Watch the Video

Design and demonstration of antenna-coupled Schottky diodes in a foundry complementary metal-oxide semiconductor technology for electronic detection of far-infrared radiation

Cite as: J. Appl. Phys. **125**, 194501 (2019); doi: [10.1063/1.5083689](https://doi.org/10.1063/1.5083689)

Submitted: 30 November 2018 · Accepted: 24 April 2019 ·

Published Online: 16 May 2019



View Online



Export Citation



CrossMark

Z. Ahmad,^{1,a),b)}  A. Lisauskas,²  H. G. Roskos,³  and K. K. O⁴

AFFILIATIONS

¹Texas Instruments, Dallas, Texas 75243, USA

²Institute of Applied Electrodynamics and Telecommunications, Vilnius University, LT-10257 Vilnius, Lithuania

³Department of Physics, Goethe University, D-60438 Frankfurt, Germany

⁴TxACE and Department of Electrical Engineering, University of Texas at Dallas, Richardson, Texas 75080, USA

Note: This paper is part of the Special Topic section published in “Advances in terahertz solid-state physics and devices,” J. Appl. Phys. **125**(15) (2019).

^{a)}Author to whom correspondence should be addressed: xeesh@umich.edu

^{b)}This research was performed while Z. Ahmad was at The University of Texas at Dallas, Richardson, Texas 75080, USA.

ABSTRACT

Electronic detection of far-infrared (FIR) radiation up to 9.74 THz is reported in a foundry complementary metal-oxide semiconductor (CMOS) technology. The detectors were fabricated with Schottky-barrier diodes (SBDs) formed in 130-nm CMOS without any process modifications. Direct-antenna matched detectors achieve a measured peak optical responsivity (R_V) of 383 and 25 V/W at 4.92 and 9.74 THz, respectively, near the 5 and 10 THz fundamental frequency of the antennas. A significantly improved R_V at 9.74 THz (25× compared to the MOSFET detectors and ~2× compared to the SBD) ensures negligible impact on the system noise-equivalent power (NEP) due to the input-referred noise of the amplifier following the detector. This work also demonstrated that by incorporating the effects of plasma resonance, transit time, and FIR absorption behavior of SiO₂, as well as the 3D electromagnetic simulations into the SBD model, good agreement between the measurements and simulations can be attained. The detector designed for a 10-THz operation achieves an optical NEP of 1.1 nW/√Hz at 9.74 THz in the shot-noise limit, which is comparable to that of commercially available pyro-detectors that are 50 000× larger.

Published under license by AIP Publishing. <https://doi.org/10.1063/1.5083689>

I. INTRODUCTION

Far-infrared (FIR) is the region of the electromagnetic spectrum that lies between THz and infrared (IR) frequencies and spans from 3 to 30 THz. Much like THz, FIR frequencies are non-ionizing in nature and bear great significance in cosmological studies.^{1–4} Cosmological studies aside, the radiation from a black body at room temperature peaks around 30 THz and is the basis of night-vision cameras and thermal imaging applications such as leak detection from buried pipes, imaging of industrial machinery,^{4,5} hot spots and tumor detection,⁶ pedestrian avoidance and

lane-control during night for automotive systems, thermal imaging of buildings to find heat escape paths,⁷ and others. Owing to great interest from the defense sector, HgCdTe (MCT) and III–V based detector technologies, capable of delivering near perfect sensitivity performance, have dominated at this frequency range.⁷ However, these detectors require cryogenic cooling leading to bulky, expensive, and inconvenient to use IR systems hindering their widespread commercial deployments. Uncooled thermal detectors such as vanadium-oxide (VOx) and amorphous-silicon (a-Si) based microbolometers require specialized fabrication as well as packaging and

suffer from slow pixel scaling, also resulting in costly solutions.^{7,8} Electronic detection using Schottky-barrier diodes (SBDs) is an attractive alternative, as it does not require thermal isolation. Since, pixel size can be potentially scaled with operating frequency (antenna size $\sim \lambda^2/4$) and no further processing beyond the standard CMOS flow is required, this approach, if made sufficiently sensitive, can provide an affordable alternative.

The speed performance improvement of CMOS technology in the past decade has attracted numerous efforts to investigate its use in millimeter-wave and THz imaging applications.⁹⁻¹³ Both Schottky-barrier diode (SBD)¹⁰ and MOSFET¹¹⁻¹³ based detectors have been investigated in various CMOS technologies (Fig. 1). Moving up to the FIR range, Boppel demonstrated the first n-MOSFET (NMOS) detectors operating up to 4.25 THz in 150-nm CMOS¹⁴ and in 90-nm CMOS^{15,16} with R_V of 11 and 230 V/W, respectively. Using third and fifth harmonic structures operating between 8 and 9 THz, measured R_V 's ranging between 0.01 and 1 V/W were also reported.^{15,17} A significant issue of low R_V detector is the resulting dependence of system performance on the noise of subsequent amplification stage typically with an input-referred noise ($v_{n,in}$) of a few nV/Hz^{1/2}. For instance, if R_V and $v_{n,in}$ are 0.01 V/W and 2 nV/Hz^{1/2}, then noise-equivalent power (NEP) will be 200 nW/Hz^{1/2}. As illustrated in Fig. 1, there is a rapid (~ 40 dB per octave) drop in the sensitivity of electronic detectors beyond 3 THz.

This paper, which is an expanded version of Ref. 18, reports the SBD electronic-detector operating at 10 THz. The detector is fabricated using an SBD in 130-nm CMOS without process modifications and achieves R_V and a shot-noise-limited NEP of 25 V/W and 1.1 nW/ $\sqrt{\text{Hz}}$, respectively. The 10-THz detector occupies an area of only 72.6 μm^2 that is 2 \times smaller than that of detectors for a state-of-the-art 12 μm microbolometer technology⁸ with $\sim 3\times$ higher operating frequency. Compared to diode-connected MOS detectors, the SBDs also have smaller pixel-to-pixel NEP variations.¹⁹

Compared to the work presented in Ref. 18, this paper explores in detail the device scaling issues faced when optimizing

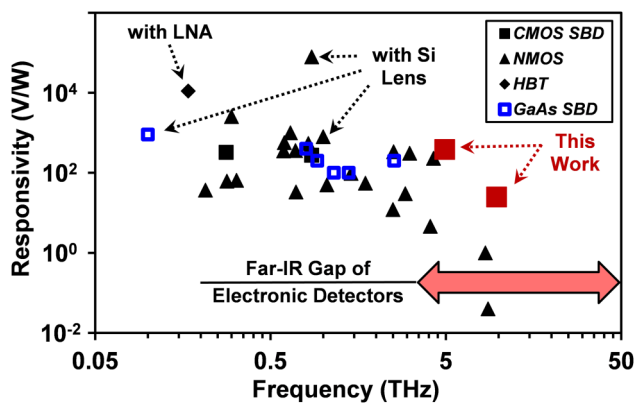


FIG. 1. The sensitivity (responsivity) performance of the state-of-the-art millimeter-wave, THz, and FIR electronic detectors fabricated in various CMOS,^{10-13,16-19} SiGe,⁴³ and GaAs⁴⁴⁻⁴⁶ technologies.

performance at FIR frequencies. A modeling approach for deeply scaled devices taking into account the carrier-inertia, plasma resonance, and transit time phenomena critical at submillimeter wave and FIR frequencies is presented. The work also provides a detailed analysis of direct resistive antenna matching technique first proposed in Ref. 18 as a solution to the nonrealizable matching network problem at these operating frequencies. The paper is organized as follows: Sec. II reviews SBD based detection basics and outlines fundamental requirements for efficient high-frequency detection. The issues associated with device scaling are discussed in Sec. III. A modeling approach valid from DC to FIR frequencies is also presented. Section IV explores design and implementation trade-offs of FIR detection structures. Measurement setup and results are presented in Sec. V. Lastly, the paper is concluded in Sec. VI.

II. SBD DETECTION AT FAR-INFRARED FREQUENCIES

An important performance metric of imaging detectors [Fig. 2(a)] is the noise-equivalent power (NEP) defined as “input power at the detector which results in a unity signal-to-noise ratio at the rectified output over a bandwidth of 1 Hz.” The NEP in the shot-noise limit for a scalable SBD [Fig. 1(b)] with “ m ” parallel cells is^{10,20}

$$\text{NEP}_{\text{shot}} = \text{NEP}_0 \left[1 + \frac{R_{s0}}{m \cdot R_j} + \frac{m \cdot R_j}{R_{s0}} \left(\frac{f}{f_T} \right)^2 \right] / \sqrt{R_j}, \quad (1)$$

where intrinsic shot-noise-limited NEP, $\text{NEP}_0 = [4nt^{1/2}(k_B T)^{3/2}]/q$, R_{s0} is the series resistance of the unit cell, R_j is the dynamic resistance of the diode, n is the diode ideality factor, f_T is the cutoff frequency of the diode at the zero-bias condition, $t_w \sim n/2$ is the white-noise temperature ratio defined as the ratio between the white noise generated from the diode and that from a resistor equal to R_j ,²¹ and k_B is the Boltzmann constant.

As previously noted in Ref. 10 and reproduced in Fig. 3(a) with m extended down to unity, the use of a smaller diode or a diode with a fewer number of unit cells in parallel can partially compensate the performance loss incurred from increased operation frequency. A further analysis performed by a linear scaling of bias current with diode size m shown in Fig. 3(b) reveals that it is possible to somewhat optimize the high-frequency performance loss with the diode size through bias optimizations. However, the necessary higher bias current would increase the $1/f$ noise corner

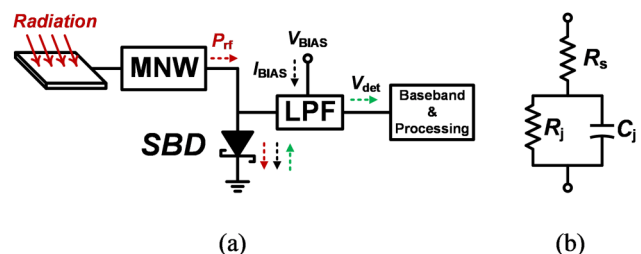


FIG. 2. (a) SBD detection (here, MNW = matching network and LPF = low-pass filter) and (b) three-element equivalent model of SBD.

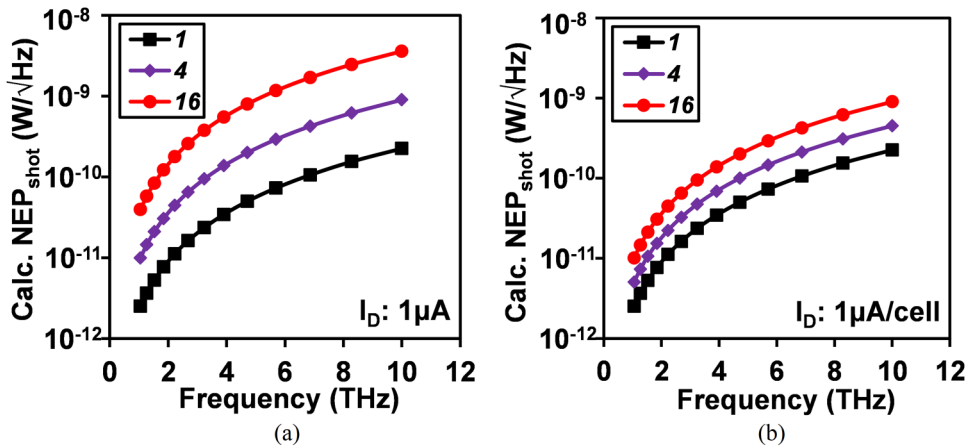


FIG. 3. Shot-noise-limited NEP behavior over frequency for varying SBD cell size, m , and (a) total I_D of $1\ \mu\text{A}$ and (b) fixed I_D of $1\ \mu\text{A}$ per cell.

frequency due to an increase in low-frequency noise requiring higher modulation frequencies for the baseband circuits (e.g., amplifier) increasing their DC power consumption. A unit-cell diode model was constructed from a linear scaling of measured 16-cell SBD parameters. The optimum value of m , $m_{opt} = \frac{R_{sh}}{R_j} \frac{f_T}{f}$, is less than unity for typical bias and FIR frequencies. From Fig. 3, it can be seen that a 1-cell SBD has 4× better NEP than a 16-cell diode at FIR frequencies between 5 and 10 THz. Therefore, a 1-cell SBD with a process-limited area of $0.4 \times 0.4\ \mu\text{m}^2$ is selected for the FIR detector implementation.

III. FIR MODELING OF CMOS SCHOTTKY DIODES

High performance Schottky-barrier diodes can be fabricated in foundry CMOS without any process modifications.^{22,23} An implant block on a diffusion region in an n-well (or p-well) defines a Schottky barrier between the cobalt disilicide (CoSi_2) and the n-well as shown in Fig. 4. A polysilicon-gate separated (PGS) SBD fabricated in a 130-nm CMOS process with an estimated f_T of ~ 2 THz was first reported in 2009.²³ The f_T is estimated from ac

measurements at 15–20 GHz of a 16-cell diode test structure with a drawn active anode cell area of $0.4 \times 0.4\ \mu\text{m}^2$.

Characterization of high-frequency phenomena such as the skin effect of series resistance, interconnect inductance, and capacitance at even upper millimeter-wave frequencies is challenging owing to the limited dynamic range of instruments and a higher contact loss. There is also the issue of validity of linear scaling used for modeling at submillimeter wave frequencies.¹⁰ A robust systematic approach to build an SBD model valid up to FIR frequencies is developed in this work. By combining the capabilities of a full-wave 3D electromagnetic (EM) simulator such as ANSYS HFSS,²⁴ physical structure modeling, and the carrier-inertia effects of a cathode important at such high operating frequencies, a scalable 1-cell FIR SBD model is constructed.

A. Series resistance

The DC value of series resistance between anode and cathode contacts of PGS-SBD can be estimated from the geometry (Fig. 4)²⁵

$$R_{s, DC} \cong R_c + \frac{R_{sh, nw}}{29} + R_{sh, nw} \frac{l_1}{4l_s} + R_{sh, n+} \frac{l_2}{2(l_s + 2l_1)}, \quad (2)$$

where R_c is the anode contact resistance, $R_{sh, nw}$ is the n-well sheet resistance, $R_{sh, n+}$ is the sheet resistance of salicided n^+ region, and l_s , l_1 , and l_2 are the dimensions shown in Fig. 4. When the parameters for the 130-nm process of Fig. 4 are used in (2), $R_{s, DC} \cong 97\ \Omega$.

An HFSS simulation was carried out on the PGS-SBD structure shown in Fig. 4 to better understand the high-frequency effects. The simulation results, shown in Fig. 5, are very close to the calculated $R_{s, DC}$ at DC and low millimeter-wave frequencies. Surprisingly, even at 5 and 10 THz, the skin effect increases the resistance by less than 5%.

B. Junction capacitance

The junction capacitance, C_j , of a uniformly doped SBD can be estimated as

$$C_j = l_s^2 \left[\frac{\epsilon q N_D}{2(\Phi_B - V_j)} \right]^{1/2} + b_1 \epsilon l_s + b_2 \epsilon \left[\frac{2\epsilon(\Phi_B - V_j)}{q N_D} \right]^{1/2}, \quad (3)$$

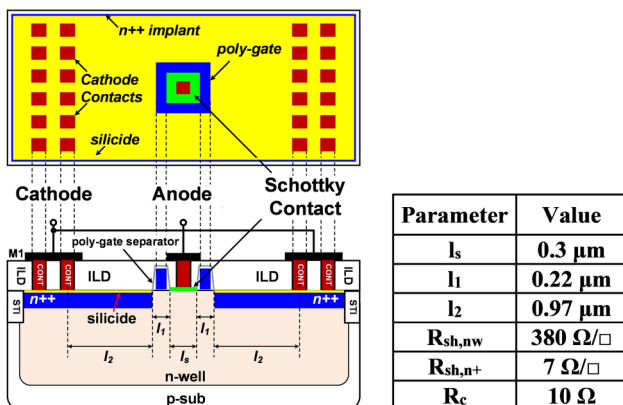


FIG. 4. Polysilicon-gate separated (PGS) SBD cross section, critical dimensions, and parameter values.

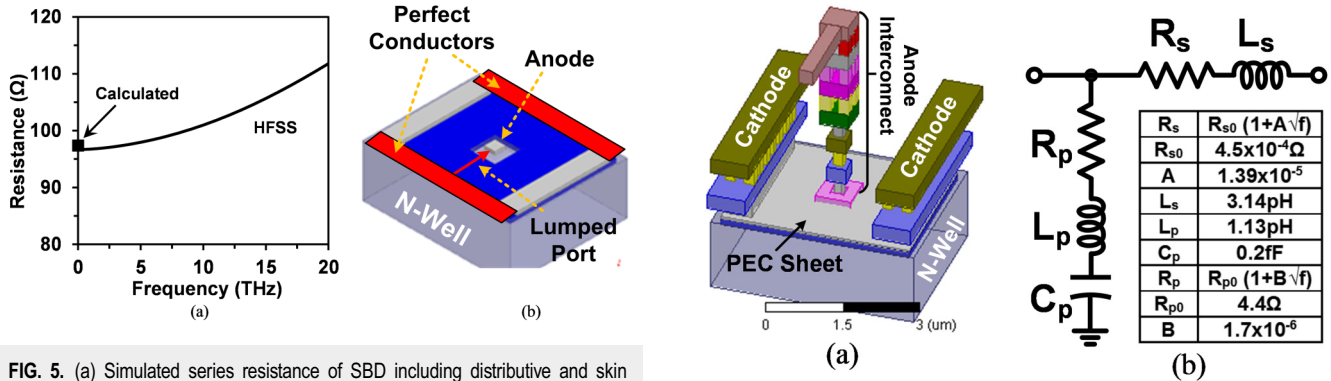


FIG. 5. (a) Simulated series resistance of SBD including distributive and skin effects. Calculated $R_{s,DC}$ is also shown. (b) HFSS port setup.

where l_s is the length of the Schottky anode, ϵ is the permittivity of the silicon, q is the electron charge, N_D is the n-well doping concentration, Φ_B is the junction built-in potential, V_j is the bias-voltage applied to the junction, and b_1 and b_2 are empirical constants equal to 1.5 and 0.3, respectively.²⁶ The first term on the right in (3) is due to the area component, while the second and third terms, respectively, take into account first and second order edge-effects for nanoscale Schottky contacts.²⁶ By substituting the values from Fig. 4 into (3) with b_1 and b_2 equal to 1.5 and 0.3, respectively, the zero bias capacitance, C_{j0} , is ~ 0.3 fF. The calculated value of C_{j0} is approximately half of that estimated from the 16-cell SBD measurements. The cause for this discrepancy is the parasitic metal-to-metal capacitances of the anode interconnect and is explained next.

C. Interconnect model

The metal interconnect (Contact-to-M6) of the SBD, shown in Fig. 6(a), couples the signal from a source, typically an antenna with a transmission line (TL), to the Schottky junction for rectification. Due to multiple thin-metal levels commonly used in submicron CMOS and nanosize anode of the diode used to improve the high-frequency performance, even properly designed interconnects lead to significant parasitics that require an accurate accounting. Unfortunately, a reasonable extraction of these parasitics through measurements is extremely challenging and sometimes beyond instrumentation capabilities as discussed earlier. Furthermore, at frequencies above 1 THz, presently, there are no commercially available network analyzers. 3D EM simulators such as HFSS can be used to fill the gap. The HFSS simulations are performed on the interconnect model shown in Fig. 6(a). A metal sheet with the perfect-electric-conductor (PEC) boundary condition was used between the anode and the cathode contacts to exclude the effects of n-well and ohmic n^+ regions already modeled in Sec. III A. The real and imaginary parts of the simulated interconnect impedance (Z_{ic}) are shown in Fig. 6(c). The imaginary component, $\Im\{Z_{ic}\}$, is predominantly inductive till the first parallel-resonance frequency (f_{r1}) at 5.5 THz caused by shunt capacitance. A second resonance (f_{r2}) of series nature occurs near 15 THz. To better understand the behavior and to mitigate the modeling challenges, a simple

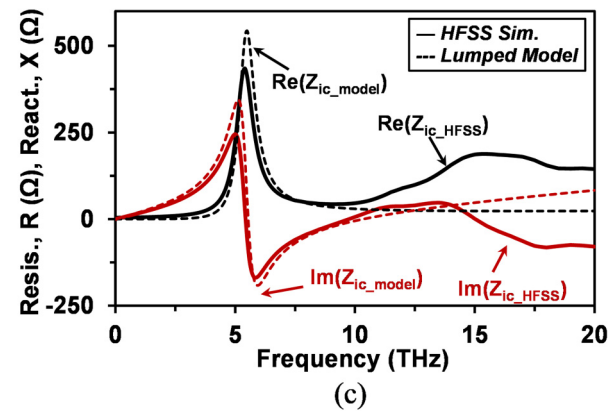


FIG. 6. SBD interconnect. (a) 3D cross section. (b) Lumped equivalent model. (c) Simulated and modeled impedance.

procedure outlined next was utilized to make an initial estimation of parasitic components: series inductance was extracted at 1 GHz with $L_s = \Im\{1/Y_{11}\}/2\pi f \approx 2.83$ pH; shunt capacitance using L_s and f_{r1} with $C_p = 1/L_s (2\pi f_{r1})^2 \approx 0.29$ fF; series inductance of C_p from f_{r2} with $L_p = 1/C_p (2\pi f_{r2})^2 \approx 0.39$ pH; series resistance of interconnect at DC with $R_{s0} = \Re\{Z_{ic}\} \approx 4.3 \Omega$. These initial values were further optimized in a circuit simulator such as Keysight Advance Design System (ADS).²⁷ A resistance R_p in series with C_p accounts for the limited Q of the shunt path, while the frequency dependency of R_s and R_p due to the skin effect was modeled as $R = R_0[1 + A\sqrt{f}]$, where R_0 is the low-frequency resistance and “A” is a fitting parameter. The SBD model including the frequency dependent R_s [i.e., $R_s(f)$], C_p , along with the broadband lumped interconnect model [parameter values given in Fig. 6(b)], is depicted in Fig. 7(a). The simulation results of the simple lumped-model in Fig. 6(c) are close to the HFSS simulations up to ~ 10 THz. Above 10 THz, the simple model starts to have noticeable errors because of the distributed nature of the structure. This is expected because the total length of interconnect, $l_i \sim 6 \mu\text{m}$, becomes equal to the guided wavelength in silicon-dioxide ($\lambda_{g, \text{SiO}_2}$) at approximately 25 THz (ϵ_r of 3.9 for SiO_2).

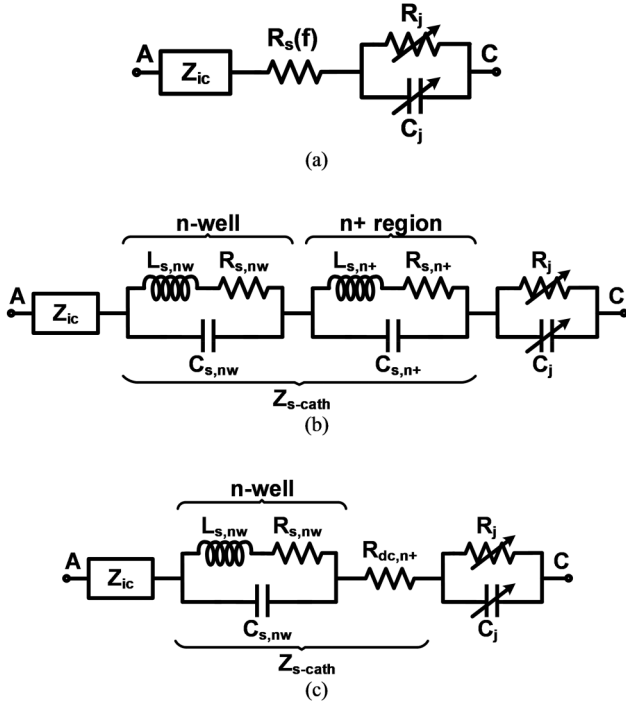


FIG. 7. FIR SBD model (a) including HFSS interconnect [Z_{ic} , Fig. 6(b)] and NW skin effect, (b) model including plasma resonance and carrier-inertia effects, and (c) final model.

D. Carrier-inertia and transit time effects at FIR frequencies

In semiconductors, charge carriers (electrons in n-doped materials such as n-well, n⁺ region, etc.) take a finite time to respond to the change in the applied electric (E) field. Due to inertia of the carriers, the applied field must slow down the carriers before their direction of motion is reversed.²⁸ This phenomenon, which appears as an inductive effect at macroscale, becomes noticeable at submillimeter frequencies. There is also the dielectric “displacement current” phenomenon. Both carrier-inertia and displacement current can be accounted for by replacing DC conductivity (σ_{dc}) used in the computation of $R_{s,DC}$ in (2) with a complex quantity,

$$\sigma_{ac} + j\omega\epsilon = \sigma_{dc} \left[\frac{1}{1 + j(\omega/\omega_s)} + j(\omega/\omega_d) \right], \quad (4)$$

where ω_s is the mean-scattering frequency of carriers approximated as $\omega_s \cong q/m^*\mu$ and ω_d is the dielectric-relaxation frequency defined as $\omega_d = \sigma_{dc}/\epsilon$. Here, once again σ_{dc} is the DC conductivity, ϵ is the permittivity of silicon, q is the electron charge, m^* is the effective mass, and μ is the mobility.

By using (4) as the high-frequency replacement of $R_{sh,nw}$ and $R_{sh,n+}$ in (2), the complex impedance^{29–31} of the cathode is

$$Z_{s,cath} \cong R_{dc,nw} \eta_{p,nw} + R_{dc,n+} \eta_{p,n+} + R_c, \quad (5)$$

where R_c is the contact resistance, $R_{dc,nw}$ is the contribution of n-well to the DC series resistance, and $R_{dc,n+}$ is the n⁺ diffusion/silicide contribution to the DC series resistance. The n-well and n⁺ plasma-correction factors, $\eta_{p,nw}$ and $\eta_{p,n+}$, respectively, are

$$\eta_{p,nw} = \left[\frac{1}{1 + j(\omega/\omega_{s,nw})} + j(\omega/\omega_{d,nw}) \right]^{-1}, \quad (6a)$$

$$\eta_{p,n+} = \left[\frac{1}{1 + j(\omega/\omega_{s,n+})} + j(\omega/\omega_{d,n+}) \right]^{-1}. \quad (6b)$$

The SBD model in Secs. III A–III C [Fig. 7(a)] can be extended to the FIR frequencies after the inclusion of the high-frequency substrate impedance, $Z_{s,cath}$, as shown in Fig. 7(b). The plasma effects [first two terms of $Z_{s,cath}$ in (5)] can be modeled using two RLC networks in series. The individual components can be represented as follows: high-frequency series resistance of the cathode, $R_{s,A} = R_{dc,A} \Re\{\eta_{p,A}\}$; inertial inductance of the cathode, $L_{s,A} = R_{dc,A}/\omega_{s,A}$; and displacement capacitance of the cathode, $C_{s,A} = 1/(R_{dc,A} \omega_{d,A})$. $\Re\{\eta_{p,A}\}$ corresponds to the real part of the plasma-correction factor, and subscripts “A” refer to “nw” in the case of n-well and “n⁺” for the ohmic-region case. The explicit dependence of the plasma-correction factor on doping can be expressed as

$$\eta_p = \left[\frac{1}{1 + j(\omega/m^*\mu(N_d)/q)} + j\left(\frac{\omega\epsilon}{N_d q \mu(N_d)}\right) \right]^{-1}, \quad (6c)$$

where N_d is the doping level and $\mu(N_d)$ is the doping dependent mobility of the material.

The classical phenomenon of “plasma resonance” occurs at the parallel-resonance frequency of the RLC network, $\omega_p = 2\pi f_p = \sqrt{\omega_s \omega_d}$. The plasma frequency ω_p is dependent on the doping level of the semiconductor and causes a substantial increase in the equivalent series resistance of the RLC network. This can be observed in the $\Re\{\eta_p\}$ plot over frequency for the varying n-type doping concentration (N_D) in Fig. 8. The curve for $N_D = 7 \times 10^{19} \text{ cm}^{-3}$ (average value) corresponds to that of the n⁺ region of the cathode. Because of high ω_p ($f_p \sim 43 \text{ THz}$) at this

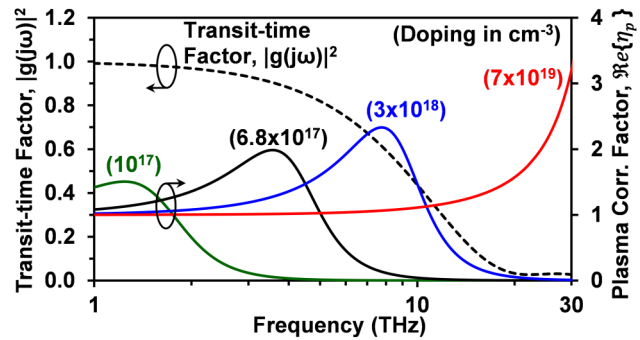


FIG. 8. Plots of real part of the plasma-correction factor $\Re\{\eta_{p,A}\}$ for varying doping concentrations and transit time degradation factor $|g(j\omega)|^2$ for N_D of $6.8 \times 10^{17} \text{ cm}^{-3}$ important for detection at and above the plasma frequency of the SBD cathode.

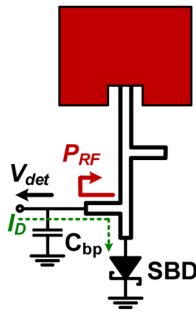


FIG. 9. Typical sub-THz imaging pixel architecture.

doping level, the $\Re\{\eta_{p,n^+}\}$ is the unity for the frequencies of interest below 15 THz. Also considering the extremely low values for L_s and C_s , and the fact that current flows mostly in the silicide region, the RLC network of the n^+ diffusion/silicide region, therefore, can be simplified to its DC equivalent as depicted in Fig. 7(c). However, the same cannot be said for the RLC network of the n-well region with a lower average doping concentration of $N_D = 6.8 \times 10^{17} \text{ cm}^{-3}$.

According to the $\Re\{\eta_p\}$ plot in Fig. 8, compared to its DC value, there is an $\sim 200\%$ increase of $R_{s,nw}$ around 4 THz which is near the estimated $f_{p,nw}$ of ~ 4.2 THz. This increase of $R_{s,nw}$ would cause performance degradation not predicted by a simple three-element model or f_T estimated from the low-frequency values of series resistance. The combined FIR model of CMOS SBD is shown in Fig. 7(c) and includes a broadband interconnect model extracted from the HFSS simulations, plasma-resonance effects in the n-well, and the skin effect related resistance increase in the cathode. An important observation from the plasma-correction factor behavior in Fig. 8 is the implied improvements in detection efficiencies above plasma frequencies. This, however, is not correct due to the transit time effects in the space-charge region at frequencies beyond f_p .^{31,32} This effect can be accounted for by a single transit time degradation factor, $|g(j\omega)|^2 = \frac{1-2c\sin(c\pi/2)+c^2}{(1-c^2)^2}$,³² where $c = \omega/\omega_p$ is the frequency normalized by the plasma frequency of the SBD cathode. The $|g(j\omega)|^2$ corresponding to the average n-well doping of $6.8 \times 10^{17} \text{ cm}^{-3}$ is shown in Fig. 8 and indicates an additional degradation of 18% and 54% at 4.92 and 9.74 THz, respectively.

IV. FAR-INFRARED PIXEL DESIGN

Two detector-operating frequencies of 5 and 10 THz were selected based on the available atmospheric propagation windows

measured using a Fourier-transform spectrometer (FTS). A typical pixel architecture employed successfully below 1 THz is shown in Fig. 9. The incoming submillimeter wave radiation captured by an on-chip antenna is delivered to an SBD through a matching network formed with grounded coplanar-waveguide (GCPW) transmission lines. The rectified signal by the SBD is then extracted across the RF bypass capacitor (C_{bp}) which is an open at modulation frequencies much smaller than RF. This pixel architecture suffers from major limitations at FIR frequencies, namely, excessive metal and radiation loss in TLs and bypass capacitors. A 10- μm long microstrip line (MSL) designed using M6 with an M2 ground plane shows a 2.4 dB of total insertion loss (IL_{tot}) in HFSS simulations at 5 THz. The radiation loss (IL_{rad}) accounts for $\sim 37\%$ of the IL_{tot} (Table I). The GCPW TLs show an improved behavior with an IL_{tot} of ~ 0.76 dB/10 μm but still suffer from excessive IL_{rad} of 0.21 dB/10 μm . At 10 THz, an integrated MSL configuration is nonrealizable. The optimized GCPW with the width and a signal-to-ground gap of 1 μm each can limit the IL_{rad} to 0.21 dB/10 μm but suffers from a significant metal loss of ~ 1.8 dB/10 μm . The losses of GCPW aside, an integrated high quality metal-oxide-metal (MOM) capacitor is required for rectified signal extraction. Figure 10(a) depicts the MOM structure optimized for FIR operation. Top and bottom plates of the MOM capacitor are realized using M6 and M1–M3 (strapped together), respectively. The HFSS simulations [Fig. 10(b)] reveal that optimized integrated MOM capacitors are usable at FIR frequencies although at the expense of radiation loss. For example, at 5 THz, the integrated capacitor suffers a radiation loss of 1.6 dB [Fig. 10(b)] in addition to that caused by the limited quality factor. By further reducing the top-plate size to $1 \times 2 \mu\text{m}^2$ (length \times width), a series-resonance frequency (SRF) of 9.1 THz can be reached at the expense of 6.7 dB of radiation loss at 9.1 THz.

Based on the above analyses, a conjugate match to the detectors at FIR frequencies of interest is problematic, and an alternate design methodology is desirable. A solution is direct-antenna-match, where the resistance of the antenna is matched (R match) to the detector input resistance.¹⁸ There are two potential issues with this approach. The first is the performance loss incurred due to the ignored reactive part of the input impedance of detector (Z_d). The parametric simulations using ADS indicate that the voltage responsivity, R_V , is lowered by ~ 0.8 dB (18%) and ~ 1.2 dB (24%) at 5 and 10 THz, respectively, compared to the lossless conjugate matching. However, using a simple single-stub matching network formed with the optimized GCPWs in Table I would result in a simulated insertion loss of 3 dB (50% lower R_V) at 5 THz and 4.5 dB ($\sim 65\%$ lower R_V) at 10 THz, which does not include the loss of integrated bypass capacitors. This indicates that the R-match approach

TABLE I. HFSS simulation results of integrated TLs. Ground plane: M1–M2.

Freq. (THz)	TL	Sig. line	Width (μm)	IL_{tot} (dB/10 μm)	IL_{rad} (dB/10 μm)	η_{rad} (%)
5	MSL	M6	3	2.4	0.4	37
	GCPW	M6	2 (Gap:1 μm)	0.76	0.21	12
10	MSL	Nonrealizable				
	GCPW	M5	1 (Gap:1 μm)	2	0.21	12

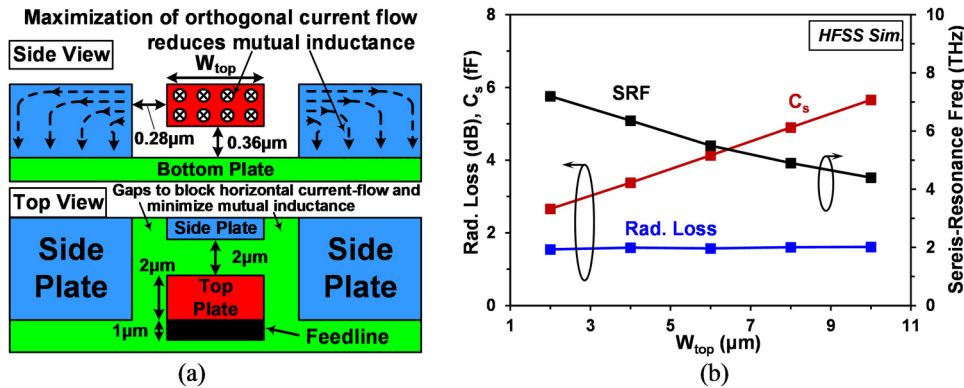


FIG. 10. On-chip MOM capacitor. (a) Top and side view of an optimized MOM structure (not to scale). Current-flow directions are also shown. (b) Simulated and calculated series-resonance frequency (SRF) and simulated radiation loss at 5 THz.

outperforms the conventional conjugate match technique by more than 2.2 dB and 3.3 dB at 5 THz and 10 THz, respectively. A second potential issue with this R-match technique is the reflections caused by nonconjugate match leading to nonoptimal imaging.³³ Nonoptimal imaging is the phenomenon of blurry images caused by the multiple reflections occurring at the poorly matched antenna of the detection structures. Figure 11 shows the simulated $|S_{11}|$ at 5 and 10 THz when the R match is used. Not only a good input match is achieved, it is also broadband in nature, which is a useful feature considering the extremely scaled devices necessary for operation at such high frequencies. The R match solves the matching difficulties of FIR detectors.

Lastly, the low-frequency rectified signal should be extracted without compromising the RF performance of the system. On-chip patch antennas have well behaved and controlled field patterns. As shown in Fig. 12, there exists a natural symmetry of the E field along the radiating edges and it goes to zero at the mid-points, creating a virtual RF ground.³⁴ This virtual ground point acts as a low-pass filter and can be tapped for DC biasing and rectified signal extraction with minimal impact on the antenna performance. At 5 THz, the HFSS simulations indicate an additional 15° tilt of the

main lobe due to unavoidable parasitics of the feed line [Fig. 13(a)]. Note that θ_{max} in Fig. 13 indicates the tilt in the main lobe, i.e., the angle where peak directivity occurs. No degradation in peak directivity (Dir) is observed. Simulations indicate only a 3° tilt of the main lobe at 10 THz [Fig. 13(b)]. Due to the non-negligible loading effect of the SBD feed line, a few degrees of main-lobe tilt are present in both antennas even before the inclusion of any DC feed or others. M7 and M6 are used to form the patch at 5 and 10 THz, respectively, with M1–M2 serving as the ground. The use of lower metal layers avoids surface-wave excitation in thicker top metals and reduces the interconnect loss by reducing the FIR signal travel path to the SBD active region. For the 10-THz patch antenna, a top-loading technique is used through an open stub placed opposite to the feed line [Fig. 13(b), inset]. This shifts the center frequency higher by approximately 8% [Fig. 13(b)]. The resulting ~17% bigger antenna aperture helps capture more FIR energy, improving SNR and partially compensating for the lower R_v at 10 THz. A minor drawback of this approach is a relatively narrow directivity bandwidth of ~1.2 THz, which is sufficient for this work.

The on-chip antennas achieve a peak directivity of 7.4 dBi at 5 THz and 8.6 dBi at 10.25 THz and are mostly limited by the

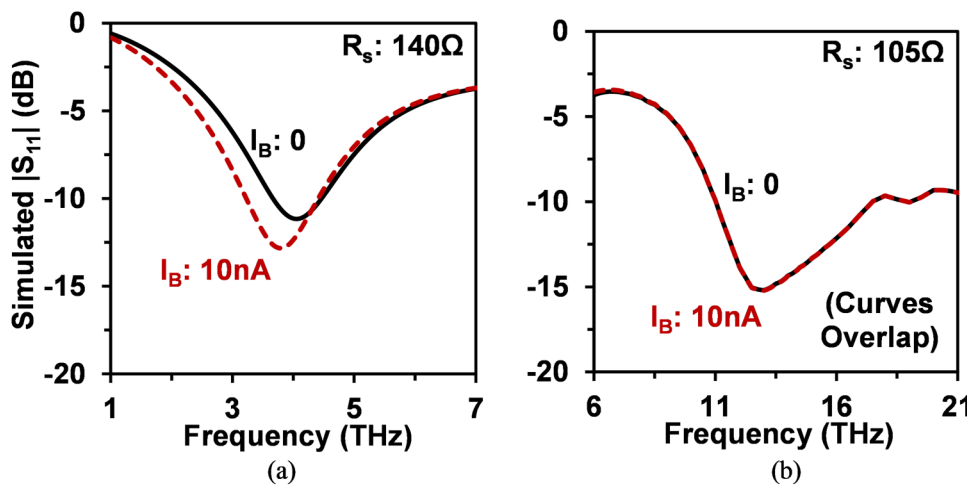


FIG. 11. Simulated input matching of R-matched FIR SBD detectors for (a) 5-THz and (b) 10-THz (curves overlap) detectors.

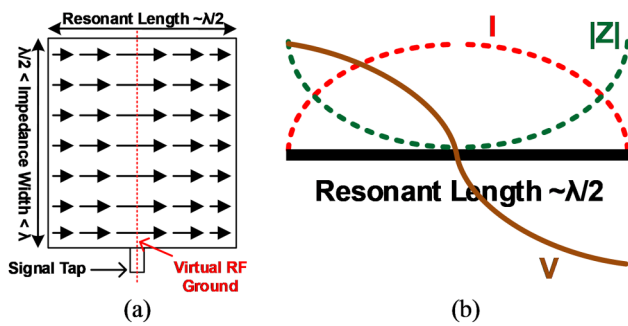


FIG. 12. (a) Current distribution on a patch antenna, (b) voltage (V), current (I), and impedance (Z) distribution with respect to the resonant length.¹⁸ Reprinted with permission from Z. Ahmad, A. Lisauskas, H. Roskos, and K. K. O, in *IEEE International Electron Devices Meeting (IEDM)* (IEEE, 2014), pp. 4.4.1–4.4.4. Copyright 2014 IEEE.

metal loss. The radiation efficiency is higher than 85%. A summary of the simulated antenna parameters is given in Table II. A typical schematic and a 3D-SBD interconnect to the patch antenna are shown in Fig. 14. The on-chip bias resistor, R_B , of 2 k Ω , further improves RF isolation.

V. RESULTS AND DISCUSSIONS

A photomicrograph of the detectors fabricated in a UMC 130-nm CMOS process is shown in Fig. 15(a).¹⁸ The detectors were characterized using a tunable free-electron-laser (FEL) source with pulse lengths up to 30 ps at the Helmholtz-Zentrum Dresden-Rossendorf (HZDR), Germany. Figure 15(b) shows the detector measurement setup including an FEL. The laser was mechanically chopped at 80 and 300 Hz, and the response was measured using a high input impedance (100 M Ω , 25 pF) low-noise amplifier (LNA) and lock-in amplifier (SR560 and SR5110). An Ophir pyroelectric camera was used for beam-profile and spot-size estimations. Figure 16(a) shows one such beam profile captured at 4.92 THz.

TABLE II. HFSS simulated integrated antenna performance.

Freq. (THz)	$L \times W^a$ (μm^2)	H^a (μm)	Peak Dir. (dBi)	3-dB Dir. BW (THz)	η_{rad} (%)
5	12×18	3.3	7.4	3.1	86
10	6.6×11	2.4	8.6	1.15	88

^aDefined in Fig. 14(b).

A calibrated Thomas–Keating (TK) absolute power meter was used for total beam-power (P_0) measurement. The power values were crosschecked with a FieldMaster power meter. Since the average laser spot size of 6.5 mm is much bigger than the FIR pixel, a peak beam intensity computed using the Gaussian-beam relation of $[2P_0/(\pi r^2)]$ instead of the average was utilized to estimate the incident power. These and simulated effective aperture area of patch antenna at the peak directivity were used to estimate the received power, which resulted in $\sim 4\times$ larger received power or $4\times$ lower responsivity compared to the values computed using the average beam intensity and physical antenna size. Figure 16(b) shows the typical DC V-I curve of the CMOS SBD.

The 5-THz detectors were characterized with laser beams at 4.29, 4.35, 4.88, and 4.92 THz. The beam attenuation was adjusted such that power between -20 and -30 dBm was incident to the antenna of detectors. This ensures operation in a small-signal detection regime. The responsivity data are shown in Fig. 17(a). The frequency response of simulated antenna gains was utilized to de-embed the effects of frequency mistuning in the originally published data.¹⁸ The responsivity shows strong frequency dependence between 4 and 5 THz, which is expected from the antenna resonance behavior. The 383 V/W optical R_V at 4.92 THz is $\sim 1.7\times$ better than that of the 4.25 THz 90-nm MOSFET detectors.¹⁶ A laser beam at 9.74 THz with incident power to the antenna of approximately -31 dBm was used to characterize the 10 THz detector. Using the peak simulated directivity of 8.6 dBi reached at 10.25 THz, an estimated optical R_V of 14.4 V/W at 9.74 THz was reported.¹⁸ However, a peak R_V of 25 V/W results when the simulated Dir. of

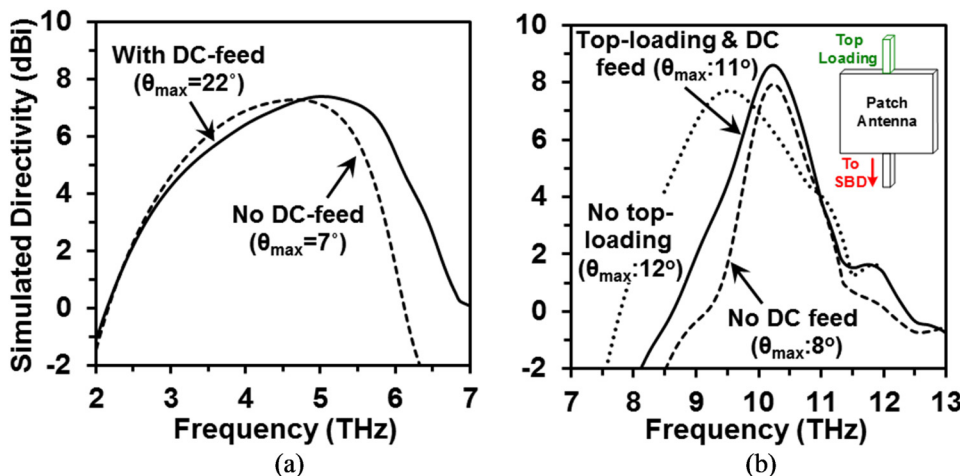


FIG. 13. Simulated impact of the DC feed line on antenna directivity (a) at 5 THz and (b) at 10 THz. A top-loading structure used at 10 THz is also shown as the inset in (b). Here, θ_{max} indicates the tilt in the main lobe, i.e., the angle where peak directivity occurs.

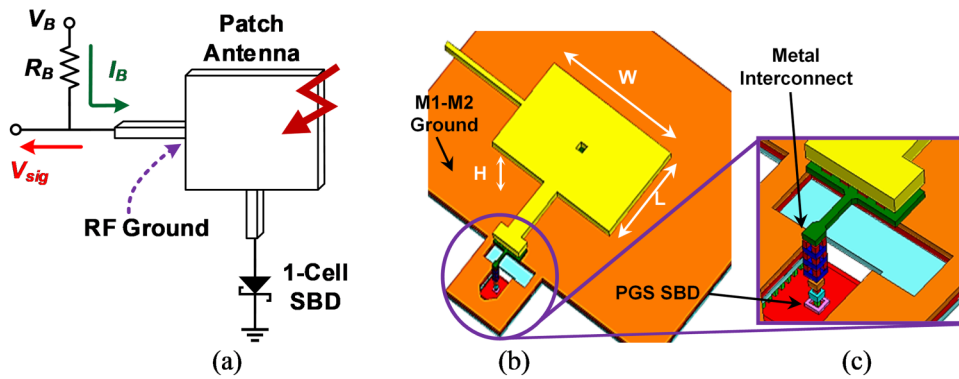


FIG. 14. (a) Schematic of the FIR detection structure, (b) 3D structure showing both on-chip patch antenna and interconnect to the Schottky-barrier diode, (c) close-up of the SBD interconnect.¹⁸ Reprinted with permission from Z. Ahmad, A. Lisauskas, H. Roskos, and K. K. O, in *IEEE International Electron Devices Meeting (IEDM) (IEEE, 2014)*, pp. 4.4.1–4.4.4. Copyright 2014 IEEE.

6.2 dBi at 9.74 THz is used without accounting for the SiO₂ absorption loss.^{35,36} This is more than 25× better than the highest reported R_V for electronic detection using the MOSFET detectors¹⁶ and ~2× compared to the SBD.¹⁸

The bias dependence of R_V is also shown in Fig. 18. The detectors show an improved response at a slightly forward biased condition due to the large zero-bias impedance of ~340 MΩ that results in voltage division with the 100-MΩ input impedance of the external LNA. At ~10 nA, the dynamic resistance drops to 2.75 MΩ with almost no degradation to the detected response. The Appendix provides a more detailed discussion on the effect of load impedance on the performance of the detector. The measured optical responsivities (Fig. 18) are 383 V/W vs the simulated peak R_V of 500 V/W at 4.92 THz and 25 V/W vs simulated 91 V/W at 9.74 THz including the plasma and transit time effects not considered in Ref. 18. The difference between the measured and the simulated R_V at 9.74 THz is further reduced by including ~40% transmission loss in SiO₂ due to operation close to 13.2 THz absorption band of SiO₂^{35,36} as well as by accounting for the non-uniform doping concentration of the n-well. This demonstrates the feasibility of design of R-matched detectors up to the FIR frequencies using augmented SBD models. A relatively larger deviation from simulations noticeable at higher bias-current conditions for the 5-THz detector is attributed to a lower high-injection knee current (I_{knee}) of ~0.2 μA for the measured 5-THz detector. The noise of the SBD detection structures at bias currents of 10,

17.3, and 700 nA is measured up to 1 MHz using an SR560 LNA and an Agilent 89441A Vector Signal Analyzer, and this is shown in Fig. 17(b). The flicker-noise corner is ~30 kHz at 17.3 nA bias with a shot noise of ~123 nV/√Hz. Based on this, the shot-noise-limited NEP of 430 pW/√Hz has been estimated at 4.92 THz. At 700 nA, the shot noise of 19.7 nV/√Hz results in an NEP of 1.1 nW/√Hz (2 nW/√Hz with Dir. of 8.6 dBi as reported in Ref. 18) for the 10 THz detector. The bias dependences of responsivity and NEP for both 5- and 10-THz detectors are shown in Fig. 18. The measured NEP of 430 pW/√Hz at 4.92 THz (first reported in Ref. 18) is ~10× worse than simulations due to a steeper degradation of R_V with the bias current explained above. Figure 18(b) also shows the simulated responsivity of the 10-THz detector without accounting for the plasma, transit time, and SiO₂ absorption effects. Compared to Ref. 18, the inclusion of these phenomena leads to a good agreement between the measured and the simulated responsivity and NEP.

Further precautions have been taken to ensure that the measured response at 9.74 THz is due to antenna-collected power and not due to spurious couplings through various mechanisms. A second potential source of error is the thermal-detection response originating from the heating of the SiO₂ layer, which, as discussed before, has an absorption band at ~13 THz. Since the patch antenna is linearly polarized, this orientation-dependence can be exploited to quantify the extent of measurement errors. Figure 19 shows one such plot. The detector output at I_{BIAS} of 0.01–0.7 μA and when the antenna

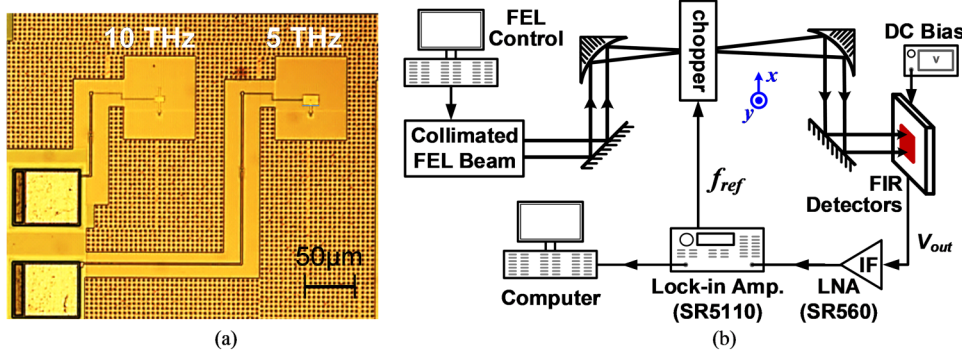


FIG. 15. (a) Die micrograph of FIR detectors.¹⁸ Reprinted with permission from Z. Ahmad, A. Lisauskas, H. Roskos, and K. K. O, in *IEEE International Electron Devices Meeting (IEDM) (IEEE, 2014)*, pp. 4.4.1–4.4.4. Copyright 2014 IEEE. (b) FIR detector characterization setup.

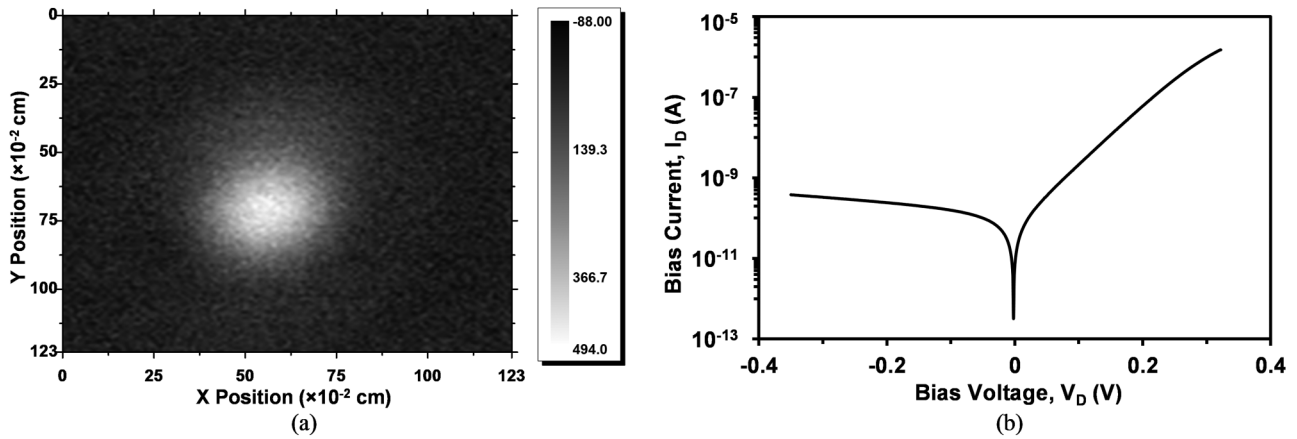


FIG. 16. (a) FEL beam profile at 4.92 THz captured using Ophir Pyrocam-III pyroelectric camera. (b) Measured DC V-I characteristics of CMOS SBD.

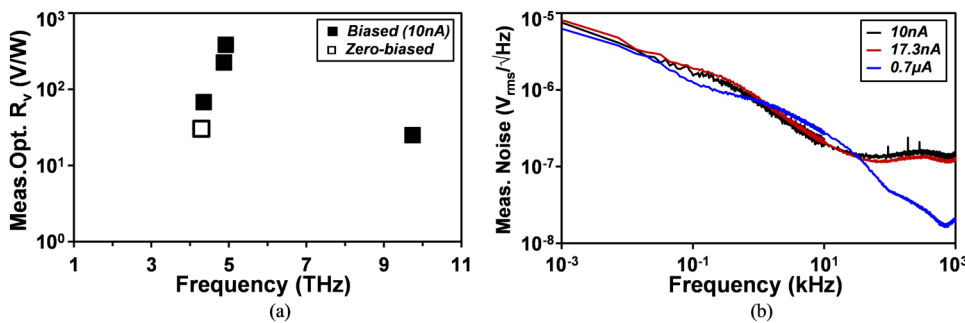


FIG. 17. (a) Measured responsivity of 5 and 10-THz SBD detection structures. (b) Measured noise at 10, 17.3, and 700 nA bias.

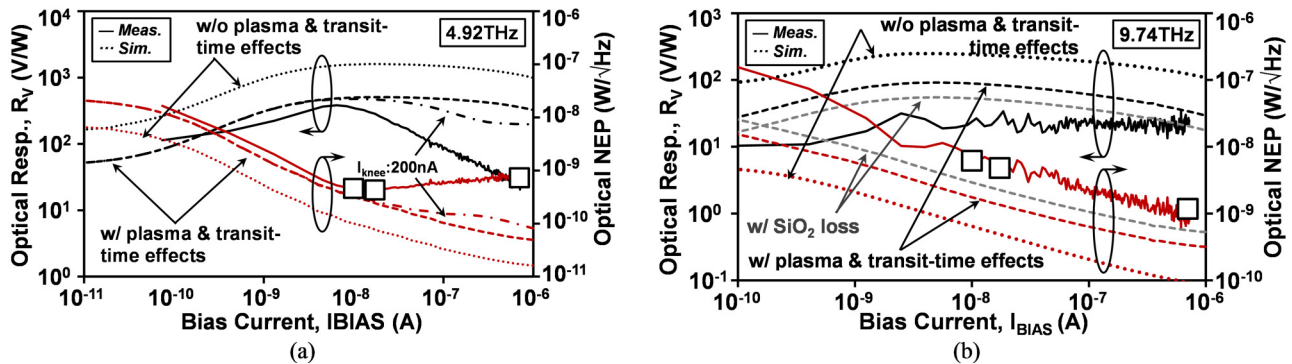


FIG. 18. (a) Measured and simulated bias dependence of responsivity and shot-noise-limited (line: noise calc., \square : meas.) NEP for the 5-THz SBD detector at 4.92 THz. Impact of high-injection knee current (I_{knee}) is also shown. (b) Simulated and measured bias dependence of responsivity and shot-noise-limited (line: noise calc., \square : meas.) NEP for a 10-THz SBD detector at 9.74 THz. Simulated R_v and NEP results after inclusion of SiO_2 transmission loss ($\sim 40\%$) due to Si-O resonance band of ~ 13.2 THz are also shown.

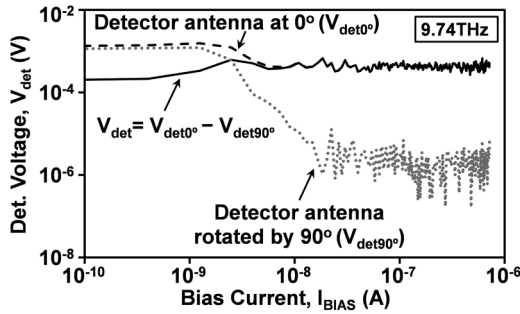


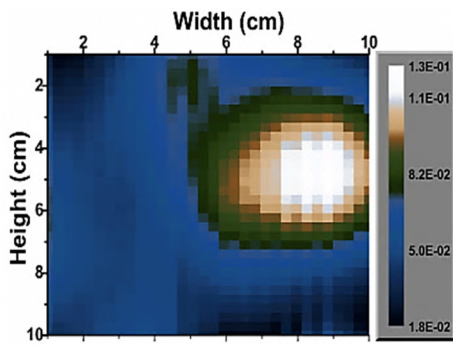
FIG. 19. Measured response of the 10-THz detector under a varying DC bias and two different antenna orientations (aligned: V_{det0° , and orthogonal: V_{det90°) with respect to the E field of the incident laser beam. Strong orientation/polarization dependence verifies the electronic nature of the detection mechanism.

polarization is aligned with the incident laser beam (V_{det0°) is more than 200× higher than when it is aligned orthogonal (V_{det90°) to it. This is a good indication that the recorded response of the 10-THz detector is due to antenna coupling. The increase in V_{det90° below 10 nA bias is due to increase in detector noise, which can also be

observed in the bias dependence of NEP in Fig. 18(b). To correct measurement errors caused by degraded NEP at low bias conditions, the R_V at 9.74 THz reported throughout this work is estimated from polarization response difference, $V_{det} = (V_{det0^\circ} - V_{det90^\circ})$, which is also plotted in Fig. 19.

Figure 20(a) shows the 10-THz detector scanned image of FIR emission from a dimmable compact fluorescent lamp (CFL).¹⁸ The FIR emission is observed only near the lowest brightness setting for the CFL. The imaging setup used is shown in Fig. 20(b) along with the THz detection board and CFL in Figs. 20(c) and 20(d), respectively.¹⁸ The almost isotropic emission from the CFL was confined to an area of ~5 mm diameter using an aluminum foil wrapped funnel resulting in an unfocused spot size of $\sim 4 \times 4$ cm² at the detector plane. The CFL spectrum was also measured using a Bruker Vertex 80v FTS to understand the CFL emission dependence on the brightness levels. The results shown in Fig. 21 under two different CFL brightness settings clearly show an almost 100× stronger emission between 8 and 30 THz at the lowest brightness setting.

The performance summary and comparison with the state-of-the-art are given in Table III. The performance of a few commercially available devices is also included as reference points. The detectors in this work have the highest optical responsivities between 4.92 and 9.74 THz for the electronic detectors. The measurement frequencies are determined by the free-electron-laser setup and may not be the optimum operation frequencies for the detectors. As noted in Sec. I, the higher R_V of the detector relaxes the input-referred noise requirements imposed on the baseband LNA following the detector, which leads to low-power consumption and a smaller die area. A metric, NEP_{LNA} , to quantify the impact of 2-nV/ $\sqrt{\text{Hz}}$ input-referred noise of a high performance LNA is computed and included in Table III. There is only a 2.8 pW/ $\sqrt{\text{Hz}}$ degradation in NEP for the 9.74-THz SBD detector with an R_V of 25 V/W compared to a 338-pW/ $\sqrt{\text{Hz}}$ NEP penalty for the harmonic detector with 0.04-V/W peak R_V between 8 and 9 THz. The 433 pW/ $\sqrt{\text{Hz}}$ of NEP at 4.92 THz¹⁸ is worse than that of the 4.25-THz NMOS detector. This is due to the steeper than expected R_V roll-off with bias current. The 1.1 nW/ $\sqrt{\text{Hz}}$ of



(a)

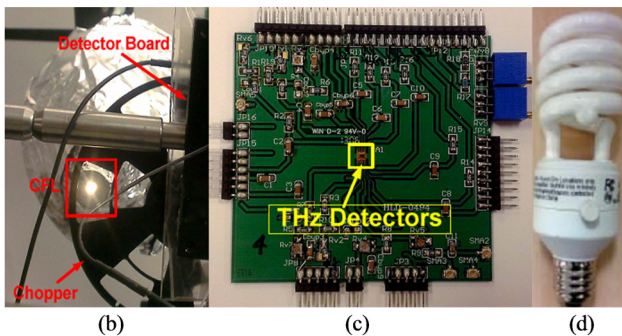


FIG. 20. (a) 2D scanned image of a compact fluorescent lamp (CFL). (b) CFL imaging setup. (c) THz detectors PCB. (d) CFL.¹⁸ Reprinted with permission from Z. Ahmad, A. Lisauskas, H. Roskos, and K. K. O, in *IEEE International Electron Devices Meeting (IEDM)* (IEEE, 2014), pp. 4.4.1–4.4.4. Copyright 2014 IEEE.

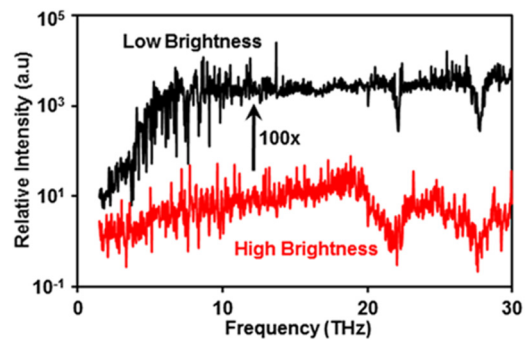


FIG. 21. Measured FTIR (Bruker Vertex 80v) spectrum of a compact fluorescent lamp (CFL) used for the imaging experiment illustrated in Fig. 20. The noise floor is higher for the trace corresponding to “low-brightness” due to lower averaging used for a stronger emission than that for a “high-brightness” setting of CFL.

TABLE III. Performance comparison.

Device	Technology	Detection mechanism	Frequency (THz)	R_V (V/W)	NEP (pW/Hz ^{0.5})	NEP _{LNA} (pW/Hz ^{0.5}) ^a	Area (μm^2)	Optics	Monolithic integration	Ref.
SBD	130-nm bulk CMOS	Electronic	4.92	383 (300 Hz)	4950 (300 Hz)	433.06	216	...	Yes	This work
			9.74	25 (80 Hz)	1100 (Shot)	1102.8	72.6	...	Yes	This work
NMOS	90-nm bulk CMOS	Electronic	4.92	383 (300 Hz)	433 (Shot)	433.06	216	...	Yes	18
			4.25	230 (30 Hz)	110 ^e	110.3	210	...	Yes	16
	150-nm bulk CMOS		8.4	0.1–1	1474 ^c	1487.5 ^c	399	...	Yes	16 and 17
			150-nm bulk CMOS	8–9	0.01–0.04	36 850 ^c	37 188 ^c	1440	...	Yes
Bolometer	VOx	Thermal	1.5–100	...	<100	...	552 ^d	Lens	Yes (additional processing)	37
Hot electron bolometer	HgCdTe		0.03–1.5	...	0.4–10 $\times 10^3$ (37 GHz) ^c	...	1.9 $\times 10^5$...	Yes (additional processing)	38
Thermopile	SiN membrane		1.6–4.3	...	1000 (<200 Hz)	...	10 ⁶	Lens	Yes (additional processing)	39
	Thin-film Bi-Sb		500 K ^e	4.1 (10 Hz)	2680 (10 Hz)	2724	4 $\times 10^6$	BaF ₂ window	No	40
	Polysilicon		500 K ^e	13.9 (10 Hz)	2504 (10 Hz)	2508	2.25 $\times 10^6$	BaF ₂ window	No	40
Pyroelectric	N/A		0.1–30	6.5 k (1 Hz) ^f	4615 (1 Hz)	IR window	No	41
Golay cell	N/A	Opto-acoustic ^g	0.02–20	10 ⁴ (12.5 Hz) ^f	10 ⁴ (12.5 Hz)	...	2.83 $\times 10^7$	PE window	No	42

^aNEP of the detector including the 2 nV/ $\sqrt{\text{Hz}}$ input-referred noise of the baseband LNA.

^bIncludes ~40% loss in SiO₂ due to operation close to the 13.2 THz absorption band.

^cNoise calculated.

^dActive area of the single pixel.

^eBlackbody radiation peaks at ~51.8 THz for this temperature.

^fWith amplifier.

^gExtremely sensitive to mechanical vibrations.

measured NEP at 9.74 THz is the lowest reported in the literature for electronic detectors and is 1.5–2.5 \times better than that of commercial pyroelectric and thermopile detectors which occupy an ~50 000 \times larger area. Additionally, the CMOS based electronic FIR detectors should be able to operate at higher modulation frequencies for video-rate imaging. The NEP of the Schottky diode detector is ~10 \times higher than that of VOx bolometers. The responsivity of Schottky diode detectors should be increased to improve NEP performance.

VI. CONCLUSIONS

This work demonstrates that electronic detection up to 10 THz is possible using Schottky-barrier diodes fabricated in CMOS with extrapolated f_T of ~2 THz. The SBD detector exhibits a 25 \times higher responsivity near 10 THz than the highest R_V previously reported using the MOSFET detectors. The inclusion of plasma and transit time effects in the n-well cathode of SBD and SiO₂ absorption improves agreements between the measurement and the simulations at FIR frequencies. This work also suggests

electronic detection beyond 10 THz and potential for affordable imaging in the FIR range using CMOS technology.

ACKNOWLEDGMENTS

This work was funded by the Texas Analog Center of Excellence (TxACE) at the University of Texas at Dallas. The authors thank Dr. M. Mittendorff for help with optics setup and HZDR Germany for FEL support. The authors thank Professor M. Lee of UT at Dallas for his gracious support for the FTIR measurements and Professor W. Frenley and Professor S. Shichijo of UT at Dallas for helpful discussions.

APPENDIX: LOAD IMPEDANCE DEPENDENCE OF THE RESPONSIVITY

The low-frequency responsivity of a square-law SBD detector with a load resistance R_L is

$$R_{VL} = \gamma_o \eta \frac{R_L}{R_L + R_j + R_s}, \quad (\text{A1})$$

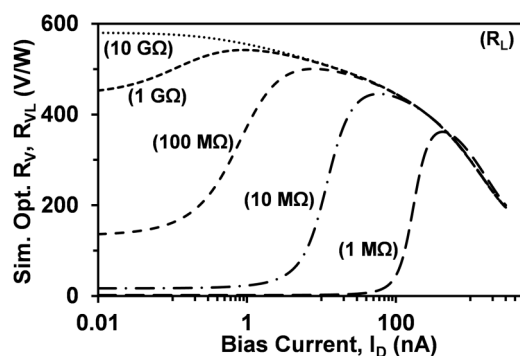


FIG. 22. Simulated optical responsivity of the 5-THz detector with swept bias (I_D) and load resistance (R_L).

where $\gamma_o = 0.5/(I_s + I_D)$ is the intrinsic voltage responsivity for a detector with a leakage current of I_s and a DC bias of I_D ,²⁰ η is the series-resistance degradation factor,²⁰ R_j is the junction resistance, and R_s is the series resistance of the detector. The required R_L to avoid response degradation decreases with I_D to satisfy the condition $R_L \gg [R_j + R_s]$, whereas the intrinsic responsivity [γ_o] degrades with I_D . These two trends lead to an optimum R_L for a given bias condition. This can be noticed in the simulated bias dependent R_V of the 5 THz detector in Fig. 22 with R_L swept between 10^6 and $10^9 \Omega$. A lower R_L shifts the R_V maxima at a higher bias condition as well as degrades the peak R_V .

REFERENCES

- E. J. Nichols and J. D. Tear, "Joining the infrared and electric wave spectra," *J. Astrophys.* **61**, 17–37 (1925).
- Leisawitz *et al.*, "Scientific motivation and technology requirements for the SPIRIT and SPECS far-infrared/submillimeter space interferometers," *Proc. SPIE* **4013**, 36–46 (2000).
- T. G. Phillips and J. Keene, "Submillimeter astronomy," *Proc. IEEE* **80**(11), 1662–1678 (1959).
- P. Siegel, "THz technology," *IEEE Trans. Microw. Theory Tech.* **50**(3), 910–928 (2002).
- M. Tonouchi, "Galore new applications of terahertz science and technology," *IEEE Trans. Terahertz Sci. Technol.* **2**, 90–101 (2009).
- J. Costello, C. McInerney, C. Bleakley, J. Selfe, and A. Donnelly, "The use of thermal imaging in assessing skin temperature following cryotherapy: A review," *J. Therm. Biol.* **37**(2), 103–110 (2012).
- A. Rogalski, *Infrared Detectors*, 2nd ed. (CRC Press, Boca Raton, FL, 2011).
- A. Rogalski, P. Martyniuk, and M. Kopytko, "Challenges of small-pixel infrared detectors: A review," *Rep. Prog. Phys.* **79**(4), 046501 (2016).
- E. Seok, D. Shim, C. Mao, R. Han, S. Sankaran, C. Cao, W. Knap, and K. K. O, "Progress and challenges towards terahertz CMOS integrated circuits," *IEEE J. Solid-State Circuits* **45**(8), 1554–1564 (2010).
- R. Han, Y. Zhang, Y. Kim, D. Kim, S. Hisashi, E. Afshari, and K. K. O, "Active terahertz imaging using Schottky diodes in CMOS: Array and 860-GHz pixel," *IEEE J. Solid-State Circuits* **48**(10), 2296–2308 (2013).
- D. Kim, S. Park, R. Han, and K. K. O, "820-GHz imaging array using diode-connected NMOS transistors in 130-nm CMOS," in *Proceedings of IEEE Symposium on VLSI Circuits, Kyoto, Japan*, 2013 (IEEE, 2013), pp. 12–13.
- E. Ojefors, U. Pfeiffer, A. Lisauskas, and H. Roskos, "A 0.65 THz focal-plane array in a quarter-micron CMOS process technology," *IEEE J. Solid-State Circuits* **44**(7), 1968–1976 (2009).
- R. Hadi, H. Sherry, J. Grzyb, Y. Zhao, W. Forster, H. Keller, A. Cathelin, A. Kaiser, and U. Pfeiffer, "A 1k-pixel video camera for 0.7–1.1 terahertz imaging applications in 65-nm CMOS," *IEEE J. Solid-State Circuits* **47**(12), 2999–3012 (2012).
- S. Boppel, A. Lisauskas, D. Seliuta, L. Minkevicius, L. Kasalynas, G. Valušis, V. Krozer, and H. G. Roskos, "CMOS integrated antenna-coupled field-effect-transistors for the detection of 0.2 to 4.3 THz," *IEEE Silicon Monolith. Integr. Circuits RF Syst.* **60**(12), 77–80 (2012).
- S. Boppel, A. Lisauskas, M. Bauer, M. Mundt, R. Venckevicius, L. Minkevicius, D. Seliuta, I. Kasalynas, B. Khamaisi, E. Socher, G. Valušis, V. Krozer, and H. Roskos, "Optimized tera-FET detector performance based on an analytical device model verified up to 9 THz," in *International Conference on Infrared, Millimeter and THz (IRMMW-THz)* (IEEE, 2013), pp. 1–1.
- A. Lisauskas, M. Bauer, S. Boppel, M. Mundt, B. Khamaisi, E. Socher, R. Venckevicius, L. Minkevicius, I. Kasalynas, D. Seliuta, G. Valušis, V. Krozer, and H. G. Roskos, "Exploration of terahertz imaging with silicon MOSFETs," *J. Infrared Millim. THz Waves* **35**(1), 63–80 (2014).
- H. G. Roskos, A. Lisauskas, S. Boppel, D. Seliuta, L. Minkevicius, I. Kasalynas, G. Valušis, B. Khamaisi, V. Krozer, and E. Socher, "THz sensing and imaging with silicon field-effect transistors up to 9 THz," in *Latin America Optics and Photonics Conference* (OSA Publishing, 2012), p. LM4A.1.
- Z. Ahmad, A. Lisauskas, H. Roskos, and K. K. O, "9.74-THz electronic far-infrared detection using Schottky barrier diodes in CMOS," in *IEEE International Electron Devices Meeting (IEDM)* (IEEE, 2014), pp. 4.4.1–4.4.4.
- D. Kim, Ph.D. dissertation, The University of Texas at Dallas, 2016.
- M. Cowley and H. O. Sorensen, "Quantitative comparison of solid-state microwave detectors," *IEEE Trans. Microw. Theory Tech.* **14**(12), 588–602 (1966).
- A. van der Ziel, "Noise in solid-state devices and lasers," *Proc. IEEE* **58**(8), 1178–1206 (1970).
- S. Sankaran and K. K. O, "Schottky barrier diodes for millimeter wave detection in a foundry CMOS process," *IEEE Electron Device Lett.* **26**(7), 492–494 (2005).
- S. Sankaran, C. Mao, E. Seok, D. Shim, C. Cao, R. Han, C. Hung, and K. K. O, "Towards terahertz operation of CMOS," in *IEEE International Solid-State Circuits Conference (ISSCC) Digest of Technical Papers, San Francisco, CA* (IEEE, 2009), pp. 202–203.
- See <http://www.ansys.com/> for more information about high frequency structure simulator (HFSS) user guide, ANSYS Inc.
- C. Mao, Ph.D. dissertation, University of Florida, 2009.
- J. Louhi and A. Raisanen, "On the modeling and optimization of Schottky varactor frequency multipliers at submillimeter wavelengths," *IEEE Trans. Microwave Theory Tech.* **43**(4), 922–926 (1995).
- See <http://www.keysight.com/> for more information about advanced design system (ads) user guide, Keysight Inc.
- K. Champlin, D. Armstrong, and P. Gunderson, "Charge carrier inertia in semiconductors," *Proc. IEEE* **52**(6), 677–685 (1964).
- K. Champlin and G. Eisenstein, "Cutoff frequency of submillimeter Schottky-barrier diodes," *IEEE Trans. Microwave Theory Tech.* **26**(1), 31–34 (1978).
- M. Kelly and T. Wrixon, "Conversion losses in Schottky-barrier diode mixers in the submillimeter region," *IEEE Trans. Microwave Theory Tech.* **27**(7), 665–672 (1979).
- T. W. Crowe, "GaAs Schottky barrier mixer diodes for the frequency range 1–10 THz," *Int. J. Infrared Millim. Waves* **10**(7), 765–777 (1989).
- A. van der Ziel, "Infrared detection and mixing in heavily doped Schottky-barrier diodes," *J. Appl. Phys.* **47**(5), 2059–2068 (1976).

- ³³R. Han, Y. Zhang, D. Coquillat, H. Videlier, W. Knap, E. Brown, and K. K. O, "A 280-GHz Schottky diode detector in 130-nm digital CMOS," *IEEE J. Solid-State Circuits* **46**(11), 2602–2612 (2011).
- ³⁴C. A. Balanis, *Antenna Theory* (John Wiley & Sons, Hoboken, NJ, 2005).
- ³⁵S. Basu, *Crystalline Silicon—Properties and Uses* (InTech, Rijeka, 2011).
- ³⁶R. Ashokan, V. Gopal, and K. C. Chhabra, "IR absorption spectra of SiO₂ films grown by photo-CVD," *Phys. Status Solidi A* **121**(2), 533–537 (1990).
- ³⁷N. Oda, A. Lee, T. Ishi, I. Hosako, and Q. Hu, "Proposal for real-time terahertz imaging system with palm-size terahertz camera and compact quantum cascade laser," *Proc. SPIE* **8363**, 83630A (2012).
- ³⁸V. Dobrovolsky, F. Sizov, V. Zabudsky, and N. Momot, "Mm/sub-mm bolometer based on electron heating in narrow-gap semiconductor," *Terahertz Sci. Technol.* **3**(1), 33–54 (2010).
- ³⁹I. Kasalynas, A. Adam, T. Klaassen, J. Hovenier, G. Pandraud, V. Iordanov, and P. Sarro, "Design and performance of a room-temperature terahertz detection array for real-time imaging," *IEEE J. Selected Topics Quant. Elect.* **14**(2), 363–369 (2008).
- ⁴⁰N. Neumann, "Comparison of pyroelectric and thermopile detectors," in *AMA Conference* (AMA Service, 2013), pp. 139–143.
- ⁴¹See <http://www.excelitas.com/> for more information about Pyroelectric detector datasheet for model LHi1128, Excilite Technologies.
- ⁴²See <http://www.mtinstruments.com/> for more information about THz goly cell detector datasheet for model SN190744. Microtech Instruments Inc.
- ⁴³E. Dacquay, A. Tomkins, K. Yau, E. Laskin, P. Chevalier, A. Chantre, B. Sautreuil, and S. Voinigescu, "D-band total power radiometer performance optimization in an SiGe HBT technology," *IEEE Trans. Microw. Theory Tech.* **60**(3), 813–826 (2012).
- ⁴⁴E. Brown, H. Kazemi, A. Young, J. Zimmerman, T. Wilkinson, J. Bjarnason, J. Hacker, and A. Gossard, "High-sensitivity, quasi-optically-coupled semimetal-semiconductor detectors at 104 GHz," *Proc. SPIE* **6212**, 62120S (2006).
- ⁴⁵J. L. Hesler and T. W. Crowe, "Responsivity and noise measurements of zero-bias Schottky diode detectors," in *18th International Symposium on Space Terahertz Technology* (National Radio Astronomy Observatory (NRAO), 2007), pp. 89–92.
- ⁴⁶See <https://www.vadiodes.com/> for more information about Schottky diode detectors, Virginia Diodes Inc.